Sensors & Actuators: A. Physical 394 (2025) 116917

Contents lists available at ScienceDirect

Sensors and Actuators: A. Physical

journal homepage: www.journals.elsevier.com/sensors-and-actuators-a-physical

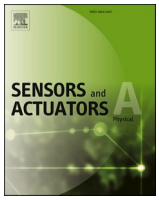

A liquid-metal-enhanced triboelectric biomimetic whisker sensor aiming at underwater flow velocity measurement and collision detection

Yuanzheng Li [a,1], Jianhua Liu [a,1], Xirui Dai [a], Xinyue Zhou [a], Tianrun Wang [a], Zinan Guo [a], Weichao He [a], Hao Jin [a], Kecheng Zhang [a], Liguo Song [a,*], Minyi Xu [a,*], Peng Xu [b,*]

[a] State Key Lab of Maritime Technology and Safety, Marine Engineering College, Dalian Maritime University, Dalian 116026, China
[b] Intelligent Biomimetic Design Lab, College of Engineering, Peking University, Beijing 100871, China

ARTICLE INFO

Keywords:
Bionic structure
Liquid metal
Triboelectric nanogenerator
Tactile sensor
Collision detection

ABSTRACT

The environmental perception capability of underwater robots is critical for enhancing their operational performance and flexibility. Inspired by the biological structure of sea otter whiskers, this paper proposes a novel sensor based on liquid metal-enabled triboelectric nanogenerators, referred to as liquid metal-based triboelectric whisker sensor (LTWS). The LTWS comprises key components, including carbon fiber tentacle, silicon capsule cover, trigger, memory alloy spring, sensing units, base, etc. The carbon fiber tentacle deflects to varying degrees in response to external forces, driving contact and separation in the corresponding sensing unit, which generates electrical signals. The LTWS exhibits high sensitivity to whisker displacement changes (7.9 mV/mm) and the output signal is basically unaffected by the touch frequency, ensuring the consistency and reliability of the signal under different operating conditions. In addition, LTWS can also be used for flow velocity measurement and collision detection in underwater environments, providing underwater robots with extended detection capabilities in low visibility and high background noise environments by purely tactile means, providing a novel method for ocean data collection.

1. Introduction

Autonomous Underwater Vehicles (AUVs) demonstrate exceptional versatility and effectiveness in contemporary subsea operations [1–4]. They can perform a variety of underwater tasks, including seabed mapping [5–7], underwater salvage [8,9], wake tracking [10–12], and pipeline inspection [13–15]. Accurate perception of the ocean environment is essential for the optimal operation of AUVs [16–18]. The environmental perception capability of underwater robots is critical for enhancing their operational performance and flexibility. In ocean environments characterized by low visibility [19] and high self-noise [20], commonly used optical detection methods [21–23] often encounter challenges such as poor image quality and blurred edges [24,25]. Meanwhile, sonar-based detection methods [26,27] are affected by phenomena like multipath effects and Doppler frequency shifts [28,29]. As a result, accurately acquiring information about the surrounding environment becomes difficult, frequently hindering the successful completion of tasks by AUVs. In such cases, underwater tactile sensing can complement detection methods like optics and sonar, enriching the environmental perception capabilities of AUVs. This enhancement allows AUVs to obtain multimodal information about the ocean. Therefore, the development of underwater tactile sensors has become an unavoidable issue.

In turbid ocean environments, where visibility is extremely low and self-noise is overwhelming, marine organisms often rely on touch to navigate and understand the complex world around them [30,31]. For example, in 2018, *Sarah McKay Strobel's* team conducted a series of interesting experiments [32]. By blocking the vision and hearing of sea otters, they discovered something remarkable: these sea otters retained the ability to skillfully track moving objects in the water. Further investigations revealed that sea otters possess highly advanced tactile sensory functions in their palms and whiskers, enabling them to effectively perceive external stimuli even in dark and turbid marine environments. As shown in Fig. 1a, when the sea otter's whisker array senses external disturbances, the whiskers activate the tactile neurons in the hair follicle structure, generating electrical signals that are transmitted

* Corresponding authors.
E-mail addresses: songliguo@dlmu.edu.cn (L. Song), xuminyi@dlmu.edu.cn (M. Xu), pengxu@pku.edu.cn (P. Xu).
[1] Yuanzheng Li, Jianhua Liu, and Xirui Dai contributed equally to this work.

https://doi.org/10.1016/j.sna.2025.116917
Received 29 June 2025; Received in revised form 18 July 2025; Accepted 26 July 2025
Available online 27 July 2025

to the brain, thereby perceiving the surrounding environment. Using this bionic principle, research teams around the world have gradually improved existing underwater tactile sensors. For example, *Xu's* team designed an underwater palm sensor inspired by the palm of a sea otter to achieve non-destructive testing of pipelines [33]; *Liu's* team designed an underwater lateral line sensor inspired by the lateral line of a fish to distinguish the type and trajectory of underwater moving objects [34]. These findings highlight that animal-inspired bionics offers a robust theoretical foundation for enhancing the structural design of underwater tactile sensors.

Triboelectric nanogenerator (TENG) is an energy harvesting and conversion technology based on the principles of triboelectric effects and electrostatic induction [35–38], capable of converting mechanical movements such as friction, compression, and vibration into electrical energy. TENG technology offers advantages including a simple structure, high sensitivity, low cost, and broad applicability, making it a promising solution for sustainable energy generation. Moreover, liquid metals, as innovative materials for sensor fabrication, exhibit a range of advantageous properties, including low density [39], high electrical conductivity [40], and exceptional stability [41]. These attributes facilitate lightweight sensor designs and enhance resistance to certain aquatic chemicals, significantly improving their stability and applicability in marine environments. Additionally, liquid metals possess excellent fluidity and flexibility, enabling them to flow and fill damaged or fractured areas for self-healing, which holds great significance in the field of flexible electronics. Thus, by integrating the triboelectric nanogenerator with liquid metal and drawing inspiration from the sea otter's whiskers [42], a novel underwater bionic tactile sensor can be devised, augmenting the AUV's capacity to perceive its surroundings effectively.

A liquid metal-based triboelectric whisker sensor (LTWS) is developed to enable tactile feedback in AUVs and to facilitate the identification of surrounding flow velocity information. As shown in Fig. 1b, the main components of LTWS include carbon fiber tentacle, silicon capsule cover, trigger, memory alloy spring, sensing units, base, etc. Even the slightest deflection of the carbon fiber tentacle prompts the trigger to move closer and compress the sensing unit in the corresponding direction, resulting in the generation of an electrical signal. The sensing unit is mainly composed of two dielectric materials: hydrogel and liquid metal composed of indium-tin alloy with a melting point of −19°C. Upon

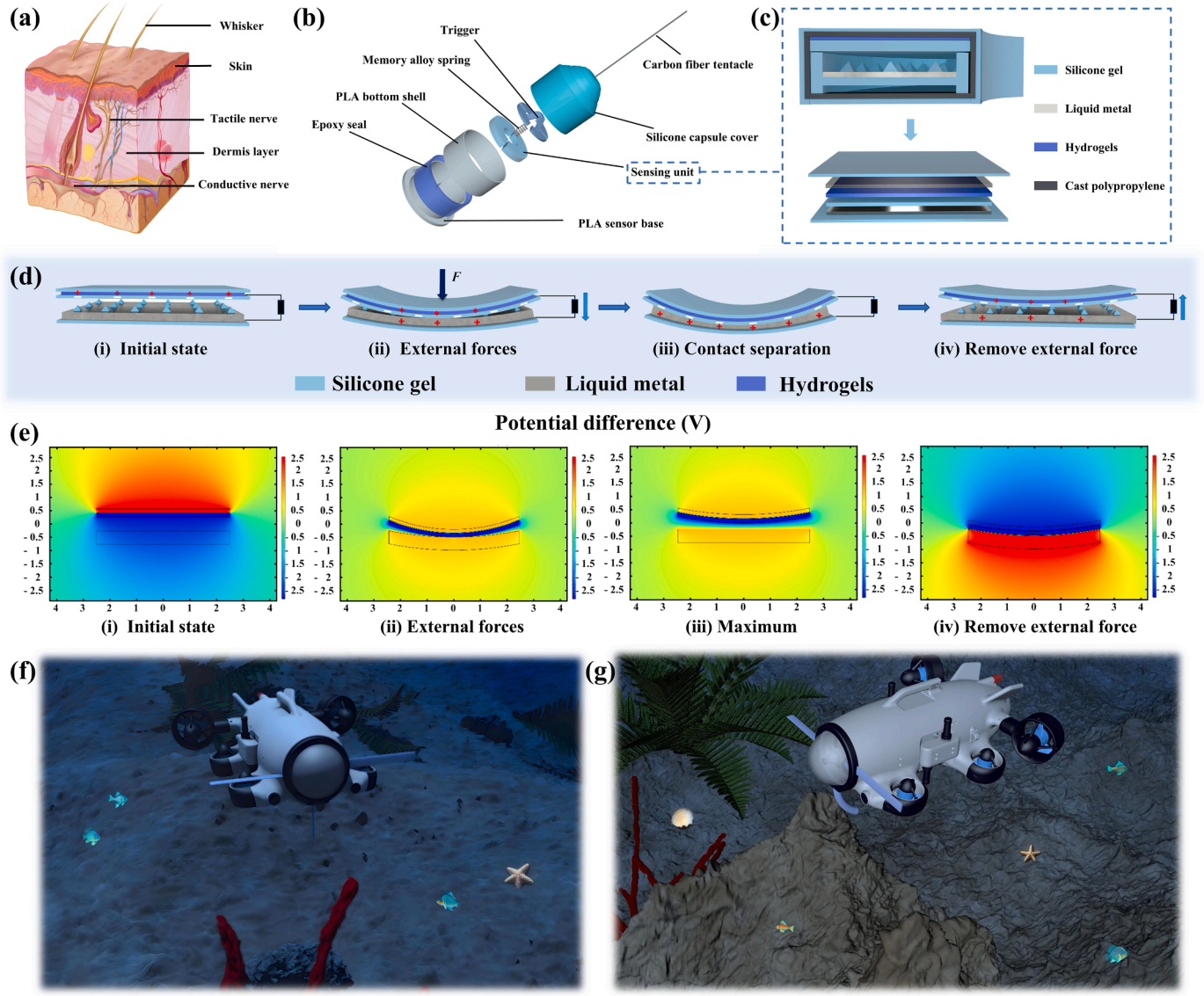

Fig. 1. The design, working principle and applications of LTWS. (a) The structure of sea otter whiskers. (b) Exploded view of the LTWS. (c) The detailed structure diagram of the sensing unit. (d) Schematic diagram of the working principle of the sensing unit. (e) Potential distribution of the sensing unit in different states. (f) The installation method of LTWS on AUVs. (g) LTWS collision avoidance application on AVUs.

the application of external mechanical stimuli, the LTWS experiences contact and separation between its dielectric layers, inducing charge transfer through triboelectric effects and electrostatic interactions, which in turn generates electrical signals. Based on the multi-channel electrical signals of the sensor unit, LTWS can estimate the flow velocity information of the surrounding flow field and enrich the underwater environment perception dimension of the AUV.

2. Results and discussion

2.1. Basic structure and working mechanism of LTWS

The LTWS captures information about underwater targets by directly contacting them using carbon fiber tentacle. Fig. 1c shows the internal structure of the LTWS sensing unit and the composition of the material layer. The upper section of Fig. 1c reveals that the LTWS sensing unit primarily comprises silicone gel, hydrogel electrode sheets, hollow chambers, and encapsulated liquid metal. The liquid metal and the top silicone layer are spaced sufficiently apart to ensure optimal contact and separation conditions. Additionally, a hollow chamber is positioned beneath the liquid metal. When external force compresses the sensing unit, the internal pressure changes, allowing the liquid metal to flow freely between the two chambers through pre-designed holes. This design prevents the liquid metal from overflowing due to excessive pressure. The blue pyramid bulge in the figure represents the microstructured triboelectric layer, which is designed to enhance the contact electrification performance of the LTWS sensing unit. Specifically, the pyramid-shaped microstructures on the surface of the silicone–hydrogel layer increase the effective contact area between the triboelectric surfaces during the bending and contact–separation process of the whisker. This structural design improves the charge generation efficiency and thus contributes to the higher output voltage and better sensitivity of the LTWS. In the lower part of the Fig. 1c, the specific material layer distribution of the sensing unit is clearly visible. From top to bottom, it consist of silicone gel layer, cast polypropylene (cpp) polymer shielding layer, positive electrode hydrogels layer, silicone gel layer, negative electrode liquid metal layer, and another silicone layer.

The working principle of the LTWS sensing unit is shown in Fig. 1d. In the state shown in Fig. 1d (i), the silicone and hydrogel surfaces carry an equal number of positive and negative charges, achieving electrostatic equilibrium. When an external load F is applied, the upper silicone and hydrogel deform and bend downward, as shown in Fig. 1d (ii). At this point, the electrostatic balance between the upper silicone and the liquid metal at the bottom is disrupted, and current flows from the hydrogel electrode to the liquid metal electrode due to the potential difference. Once the liquid metal layer tightly adheres to the upper silicone, the charge transfer is complete. The contact interface between the liquid metal and the upper silicone reaches an electrostatic equilibrium, similar to the equilibrium achieved after charge transfer due to the triboelectric effect during the first contact, as shown in Fig. 1d (iii). Furthermore, because the silicone undergoes elastic deformation, upon removal of the external load, it produces an outward elastic force that causes the silicone to revert to its original shape, as illustrated in Fig. 1d (iv). When the upper silicone and the liquid metal separate, the electrostatic balance between their surfaces is disrupted again, creating a potential difference. Under the influence of electrostatic induction and the potential difference, current flows from the liquid metal to the upper hydrogel electrode, ultimately returning to the initial state shown in Fig. 1d (i). This completes one cycle, and with repeated external loading, the sensing unit can generate alternating current output.

Utilizing finite element analysis, the potential distribution of the LTWS sensing unit under different states was simulated using COMSOL Multiphysics software within the framework of Maxwell's equations, and the corresponding potential distribution was quantitatively evaluated. The potential distribution of the LTWS sensing unit in different states is shown in Fig. 1e. In four different states, when external loads are applied to the LTWS sensing unit from different directions, it undergoes elastic deformation, generating a potential difference and causing charge transfer to balance the potential difference. Once the external load is released, the LTWS sensing unit returns to its initial state, and the charge distribution also returns to its initial state. The electrostatic simulation results of the LTWS sensing unit are consistent with theoretical calculations and working principles, further verifying the accuracy of the electrostatic model of the LTWS sensing unit.Fig. 1f illustrates the installation method of the LTWS on AUVs. Analogous to the whiskers of a sea otter, the LTWS can be strategically mounted on both sides and the underside of the AUV's front section, facilitating continuous acquisition of environmental data as the AUV navigates through marine environments. Fig. 1g demonstrates the application of LTWS in collision avoidance for AUVs. During underwater operations, AUVs encounters environments characterized by complex terrain structures and numerous obstacles. The integration of LTWS enables the AUV to detect the positions of nearby objects in real time, facilitating rapid responses to potential collisions. This capability significantly enhances the AUV's navigational precision and operational efficiency while reducing the likelihood of equipment damage, ensuring safer and more reliable mission execution.

2.2. Materials selection and theoretical modeling of LTWS

As the core component of a TENG, the choice of triboelectric layer materials directly determines the output performance of the sensing unit. The triboelectric series of materials commonly employed in the laboratory to construct nanogenerators is presented in Supplementary Material S1. Greater signal output is observed when the dielectric material nearer the bottom contacts that nearer the top. This phenomenon arises because materials with higher electronegativity more readily attract electrons during electrode contact, thereby producing larger output signals from the sensing unit. In this section, several electrode materials were evaluated, including aluminum, silicone gel, copper, ink-FEP film, and liquid metal–hydrogel electrodes. Fig. 2a illustrates their open-circuit voltages under identical experimental conditions, demonstrating that the ink-FEP film and liquid metal–hydrogel electrodes deliver superior performance. To facilitate an intuitive comparison of the output performance between the conductive ink–FEP film electrode and the liquid metal–hydrogel electrode, further comparative tests were conducted. As shown in Fig. 2b, under identical external load and frequency conditions, the liquid metal–hydrogel electrode exhibits both a higher output signal and a faster response time. This enhancement is attributed to the ability of liquid metal to form a low-impedance solid-liquid interface with the hydrogel, owing to its high conductivity and fluidity, which reduces contact resistance. The hydrogel's porous structure further accelerates charge transfer via ion migration and reduces polarization effects. In contrast, the conductive ink–FEP film impedes charge transfer due to the high interface impedance between the rigid matrix and conductive particles, as well as microcracking under dynamic load. Additionally, the double-layer capacitance effect of the liquid metal–hydrogel interface further enhances the transient response speed. Fig. 2c illustrates the specific percentage increase in output signal and response time for the liquid metal–hydrogel electrode, with improvements of 33.8 % and 28.9 %, respectively, compared to the conductive ink–FEP film electrode. In addition, durability tests were conducted on both the conductive ink–FEP film electrode and the liquid metal–hydrogel electrode, with an experimental load of 5 N and a frequency of 1 Hz. The results, as shown in Fig. 2d, demonstrate that both electrodes exhibit excellent stability. Under long-term operational conditions, no significant performance degradation or structural failure occurred, ensuring stable electrical output under prolonged mechanical stimulation.

To facilitate a clearer understanding of the movement of the LTWS whisker under external loads, it is essential to develop a dynamic model that captures the bending deflection of the whisker. Prior to formulating

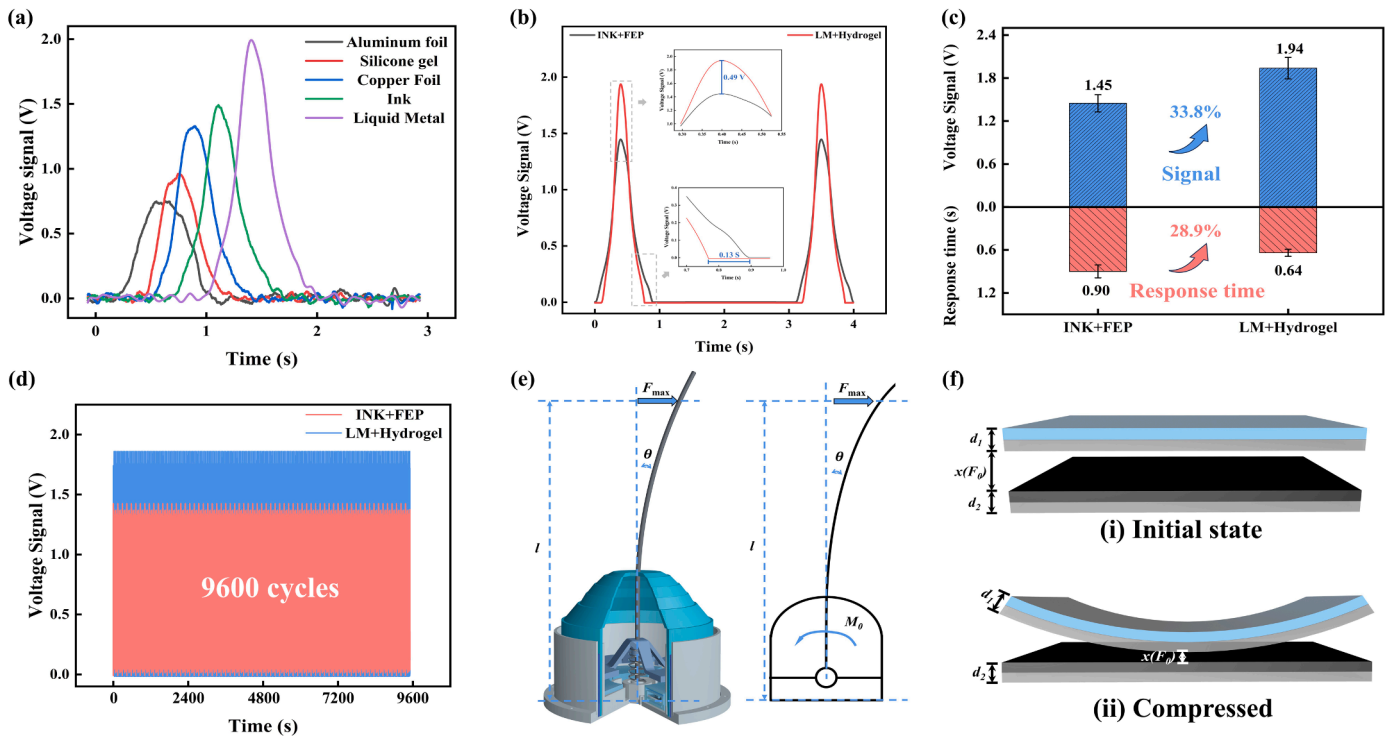

Fig. 2. Materials selection and theoretical modeling of LTWS. (a) Open-circuit voltages of five electrodes under the same experimental conditions. (b) Intuitive output performance comparison between conductive ink–FEP film and liquid metal–hydrogel electrode under the same conditions. (c) Schematic diagram of specific improvement of output signal and response time. (d) Durability test results of conductive ink–FEP film and liquid metal–hydrogel electrode. (e) Schematic diagram of the mechanical structure of LTWS. (f) Schematic diagram of parameters of the triboelectric layer of the sensing unit.

the theoretical model, two assumptions are made: (1) The whisker experiences a brief duration of force application. (2) The axial deformation of the whiskers is small. Based on these assumptions, the vibration dynamics of the biomimetic whisker are modeled using the undamped Euler-Bernoulli beam theory, which assumes a uniform cross-section. In this model, axial strain and cross-sectional rotation are considered negligible compared to shear strain, as illustrated in Fig. 2e. This approach is appropriate for slender beams where shear deformations are insignificant, and the beam's cross-section remains plane and perpendicular to the neutral axis during deformation. In the figure, l is the distance that F_{max} acts on the carbon fiber tentacle, F_{max} is the force acting on the tentacle, θ is the rotation angle of the tentacle under the action of F_{max}, and M_0 is the bending moment of the tentacle under the action of F_{max}. For the initial analysis of hydrodynamic loading conditions, we begin by modeling the LTWS system exclusively subjected to underwater fluid interactions. The governing equation describing the vibrational behavior of an undamped Euler-Bernoulli beam can be expressed as:

$$EI\cdot\frac{\partial^4 w(x,t)}{\partial x^4}+c_s I\cdot\frac{\partial^5 w(x,t)}{\partial x^4\partial t}+c_a\cdot\frac{\partial w(x,t)}{\partial t}+m\cdot\frac{\partial^2 w(x,t)}{\partial t^2} = -F_{\max}(l-x) \tag{1}$$

Where: E is Young's elastic modulus; c_s is the damping strain rate equivalent coefficient of the beam; c_a is the fluid damping coefficient; $w(x,t)$ is the displacement of the tentacle rod in the direction of flow velocity; m is the mass density of the tentacle; and I is the second-order moment of the cross-sectional area of the tentacle.

Under the condition that the beam boundary is free, the characteristic equation can be expressed as:

$$\varphi_r(x)=\sqrt{\frac{1}{ml}}[\cos\frac{\lambda_r}{l}\cdot x-\cosh\frac{\lambda_r}{l}\cdot x+\frac{\sin\lambda_r-\sinh\lambda_r}{\cos\lambda_r+\cosh\lambda_r}\left(\sin\frac{\lambda_r}{l}\cdot x-\sinh\frac{\lambda r}{l}\cdot x\right)] \tag{2}$$

Where λ_r is the dimensionless frequency number, which can be obtained from equation $1+\cos\lambda_r\cosh\lambda_r=0$.

Then, when the tentacle is in physical contact with the underwater obstacle, F_0 acts on the l on the tentacle rod at time t, and the bending moment of the cross section at the force point of the tentacle can be written as:

$$M(x)=-F_0(l-x)(x<l) \tag{3}$$

According to material mechanics, the approximate differential equation of the deflection curve is:

$$\frac{\frac{d^2w}{dx^2}}{\left[\left(1+\left(\frac{dw}{dx}\right)^2\right)\right]^{\frac{3}{2}}}=\frac{M(x)}{EI} \tag{4}$$

Since the bending deformation of the tentacles under the action of F_0 is small, it is similar to the case of small deflection. $\left(\frac{dw}{dx}\right)^2<<0$, at this time, Eq. (4) can be simplified to:

$$M(x)=\mathrm{EI}w(x,t)''=-F_0(l-x) \tag{5}$$

The deflection curve equation obtained by quadratic integration is:

$$Elw=\frac{F_0x^3}{6}-\frac{F_0lx^2}{2}+C_1x+C_2 \tag{6}$$

Where: w represents the deflection of the tentacle under the action of F_{max}; C_1 and C_2 are constant terms.

By substituting the boundary conditions of the undamped Euler–Bernoulli beam into the governing equation, the constants C_1 and C_2 can be determined. The deformation state of the tentacles under the action of F_0 can be obtained, and the deformation state of the tentacles directly determines the degree of contact and separation of the sensing unit. As illustrated in Fig. 2f, let the thickness of the upper triboelectric

layer be denoted as d_1 and the lower triboelectric layer as d_2.The interlayer distance $x(F_0)$ between the two triboelectric layers varies with the applied force F_0. Upon contact between the upper silicone layer and the liquid metal layer, opposite static charges of equal density are induced on their surfaces. When $x(F_0)$ changes with the magnitude of F_0, an induced potential difference V will be generated between the two electrodes. This potential difference will drive the transfer of electrons in the external circuit. Let the charge transfer amount be Q. In actual experiments, the side length S of the triboelectric layer material is much larger than the sum of $d_1 + d_2 + x(F_0)$. Therefore, it can be assumed

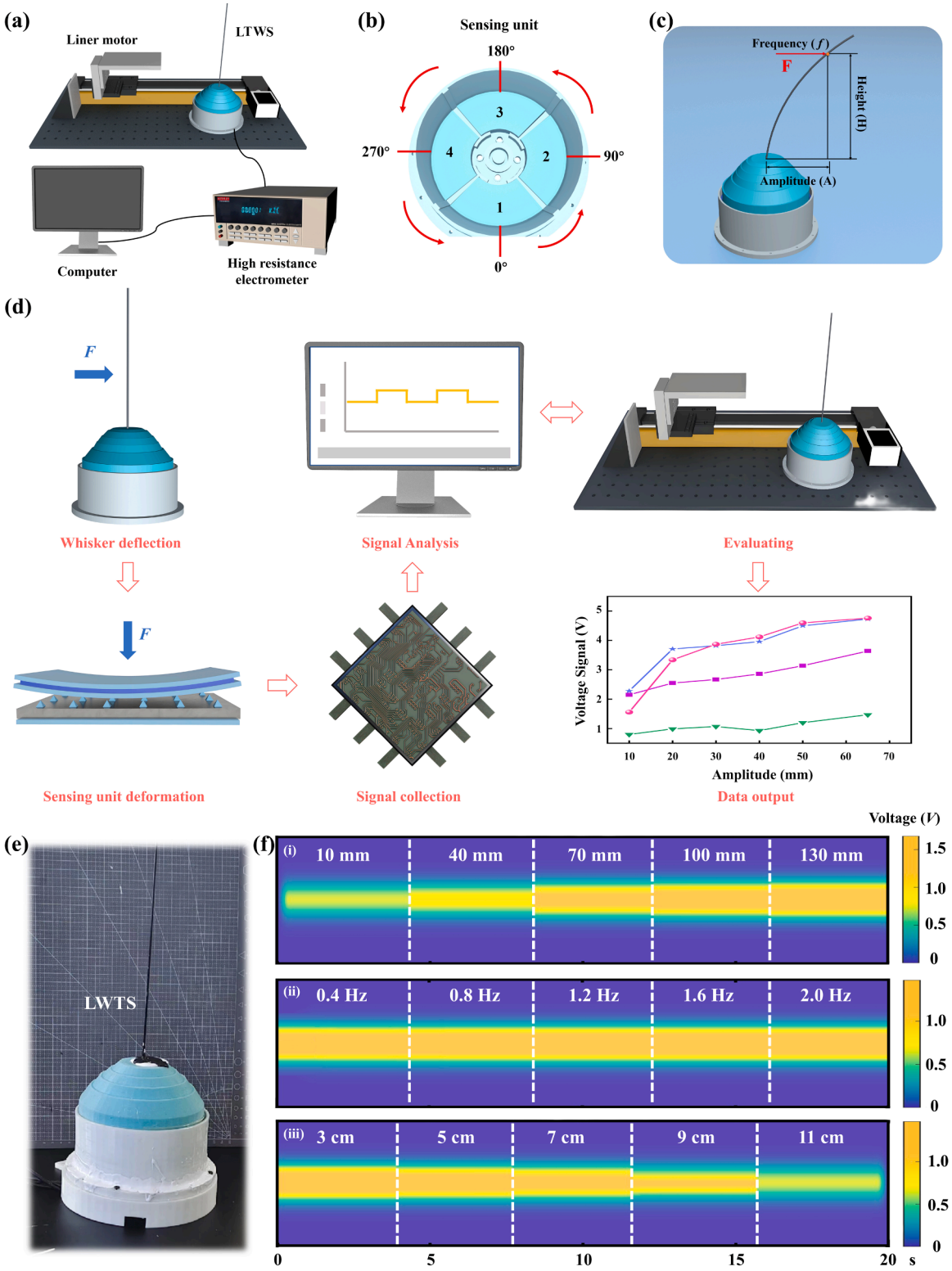

Fig. 3. Materials selection and theoretical modeling of LTWS. (a) The test bench of LTWS. (b) The placement and angle of the LTWS sensing unit. (c) The touch parameter definition of LTWS. (d) Electromechanical conversion schematic diagram of LTWS. (e) Actual physical diagram of LTWS. (f) Heat map of the effects of deflection amplitude, touch frequency, and touch height on the output of the LTWS.

that S is infinite. According to the deduction of this situation by Niu et al., it can be known that:

In the upper triboelectric layer:

$$E_1 = -\frac{Q}{S\varepsilon_0\varepsilon_1} \tag{7}$$

In the air gap:

$$E_0 = \frac{-\frac{Q}{S} + \sigma(t)}{\varepsilon_0} \tag{8}$$

In the lower triboelectric layer:

$$E_2 = -\frac{Q}{S_{\varepsilon_0\varepsilon_2}} \tag{9}$$

Where: E_n (n = 0, 1, 2) is the potential difference, ε_0 is the relative dielectric constant of air, ε_1 is the relative dielectric constant of silicone, ε_2 is the relative dielectric constant of liquid gold; $\sigma(t)$represents the charge density. So the potential difference between the electrodes can be expressed as:

$$V = E_1 d_1 + E_2 d_2 + E_0 x(F_0) \tag{10}$$

Combining the above formulas, the V- Q- $x(F_0)$relationship of LTWS can be obtained as follows:

$$V = -\frac{Q}{S\varepsilon_0}\left(\frac{d}{\varepsilon_1} + \frac{d_2}{\varepsilon_2} + x(F_0)\right) + \frac{\sigma x(F_0)}{\varepsilon_0} \tag{11}$$

From Eq. (11), it is evident that the induced potential difference V, the charge transfer amount Q, and the distance $x(F_0)$ between the triboelectric layers are directly related. In the experiment, the sensor material has been determined and the thickness of the upper friction layer d_1 and the thickness of the lower friction layer d_2 are both constants, which means that the deformation state of the tentacles directly affects the output voltage and charge of the LTWS, which provides ideas and directions for the next experimental plan.

2.3. Output characterization of LTWS

In the experiment exploring the output characteristics of the LTWS, a method involving active collisions between obstacles and the tactile sensor was employed for testing. The LTWS is mounted on a linear motor platform, and the linear motor is used to load obstacles to collide with the tentacle of the LTWS and set different contact offset amplitudes, touch height, touch frequency, touch direction and other experimental parameters to effectively simulate the active contact process of short contact between LTWS and external objects, small contact stress and short contact time, and then explore the impact of the above parameters on the output characteristics of LTWS. The signal of the LTWS sensing unit is exported through four shielded wires, measured using *KEITHLEY 6514* electrometer and *NI-6259* acquisition card, and the *LabVIEW* visualization program is used to transmit the electrical signal collected by the electrometer to the computer *LabVIEW* interface for display in real time, as shown in Fig. 3a.

The LTWS consists of four sensing units, arranged as shown in Fig. 3b. The four sensing units are axially symmetric and mounted on the base of the LTWS, arranged in a counterclockwise sensing unit 1, sensing unit 2, sensing unit 3 and sensing unit 4. During the experiment, the influence of the touch direction parameters of the whiskers needs to be tested. Therefore, when the external load F_x acts on the whiskers, if the deflection direction of the whiskers is the radial direction from the center of the base to the sensing unit 1, the touch direction is defined as 0°, and the directions corresponding to the sensing units 2, 3 and 4 are defined as 90°, 180° and 270°, respectively. As presented in Fig. 3c, in order to facilitate the use of each touch parameter, assuming that the linear motor loaded object touches the tentacle with an external load of F_x, the length projected in the vertical direction between the touch position and the top center of the silicone capsule cover is defined as the touch height H, and the length projected in the horizontal direction between the touch end position and the top center of the silicone capsule cover is defined as the touch offset amplitude A, and the frequency of the object touching the tentacle is defined as the touch frequency f.

The LTWS can convert the mechanical motion of carbon fiber tentacle into electrical signals, enabling the establishment of a corresponding electromechanical conversion model. The principle is illustrated in Fig. 3d. When an external force F acts on the carbon fiber tentacle, the mechanical motion exerts a force on the internal sensing unit, initiating a contact-separation process within the unit, thereby generating electrical signals. By connecting an external signal collection device, these electrical signals can be transmitted to a computer in real time for data analysis. Once the data processing is complete, subsequent experimental evaluation is conducted to verify the authenticity and reliability of the final output data. Fig. 3e is the actual physical photo of LTWS.

Fig. 3f presents a heat map illustrating the effects of whisker deflection amplitude A, touch frequency f, and touch height H on the output signals of the LTWS. Taking sensing unit 1 as the subject of investigation, the impact of touch offset amplitude on the output characteristics of the LTWS is examined. The touch frequency f is fixed at 1.0 Hz, the touch height H is 11 cm, and the touch direction is 0°. The touch offset amplitude A is changed, and open circuit voltage of the sensing unit 1 are measured at A = 10 mm, 40 mm, 70 mm, 100 mm, and 130 mm. The effect of the touch offset amplitude A on the output voltage signal of the sensing unit 1 is shown in Fig. 3f (i). According to the heat map, it can be inferred that when the offset amplitude A gradually increases from 10 mm to 130 mm, the voltage signal output increases synchronously, reaching 1.67 V at 130 mm. This is because the increase in the touch offset amplitude increases the pressure applied by the tentacle to the sensing unit 1 through the trigger, as the deformation of sensing unit 1 grows, the contact separation between the silicone and the liquid metal increases, resulting in a higher output voltage that corresponds to the increase in offset amplitude A. By substituting the experimental data into the sensitivity S formula, the sensitivity of the LTWS is determined to be 7.9 mV/mm.

$$S = \frac{\Delta V}{\Delta A} \tag{12}$$

However, Fig. 3f (ii) shows that when the parameters such as amplitude A, angle 0°, and height H are fixed, the voltage value will not increase with the increase of frequency. This is because the increase in frequency does not affect the degree of contact separation. The minimum distance between the positive and negative electrodes remains constant, so the voltage remains unchanged. The effect of the touch height H on the output voltage signal of the sensing unit 1 is shown in Fig. 3f (iii). When the touch height is 3 cm, the output voltage is the largest, reaching 1.6 V. This is because under the same touch offset amplitude A, the lower the touch height H, the greater the pressure applied by the whisker to the sensing unit 1 through the trigger, which leads to a greater output voltage of the sensing unit. When the touch height gradually increases, the voltage output decreases. This is because as the touch height increases, the actual displacement generated by the whisker driving the trigger becomes smaller, which reduces the pressure applied by the trigger on the sensing unit 1, thereby reducing the output voltage.

3. Applications of LTWS

3.1. Application of LTWS in direction recognition

Keeping other parameters constant, the impact of touch direction on the output characteristics of sensing unit 1 is shown in Fig. 4a (i). For sensing unit 1, the maximum voltage output appears in the 0° direction, and its load sensitivity to the 0° direction is significantly higher than to

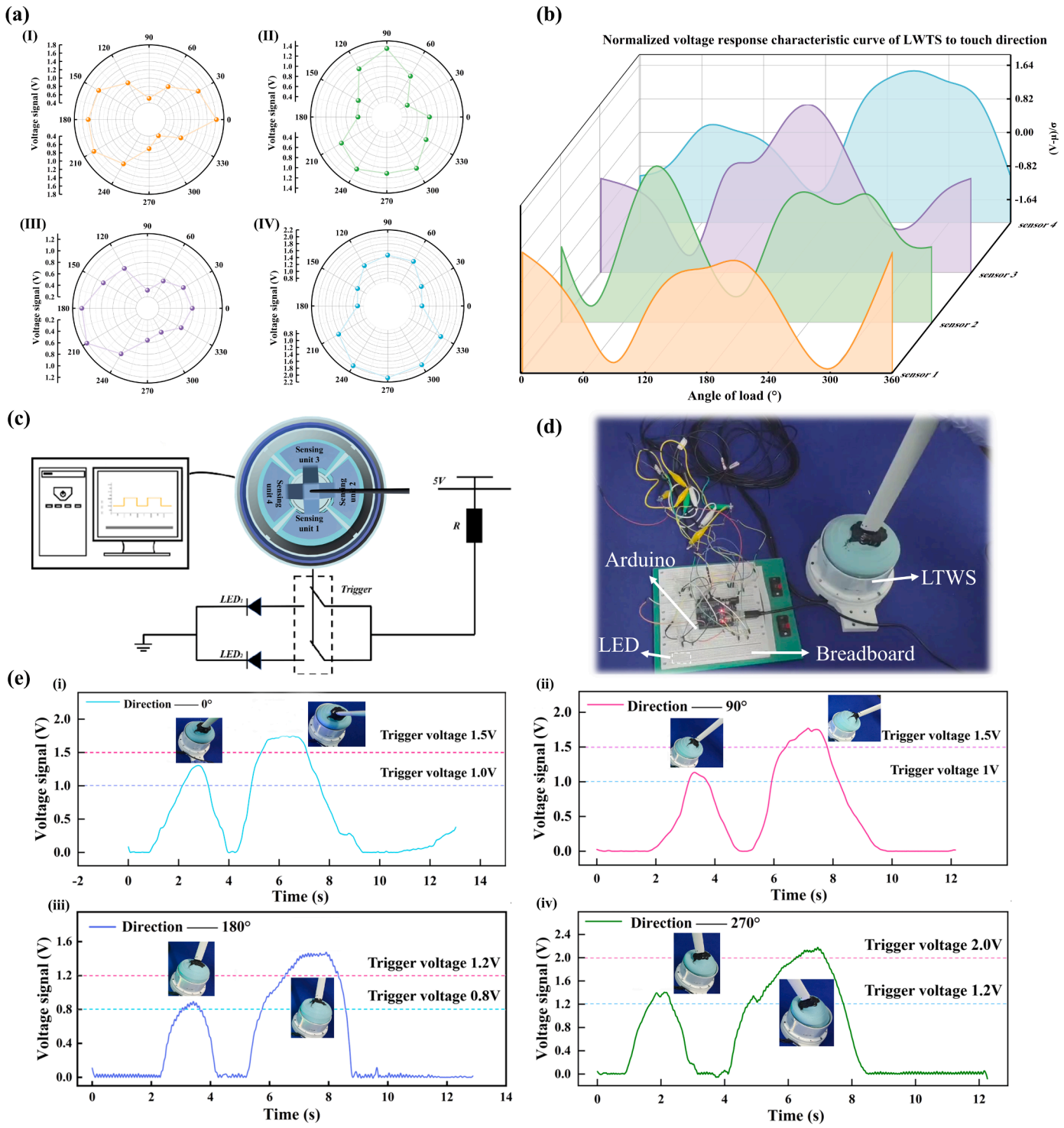

Fig. 4. Application of LTWS in direction recognition. (a) The influence of touch direction θ on the output characteristics of the sensing unit. (b) Normalized voltage response characteristic curve of LTWS to touch direction. (c) Equivalent circuit diagram for real-time threshold control of LED light status. (d) The test bench of LTWS real-time control. (e) The real-time control voltage diagram of LTWS.

other directions. The impact of touch direction on the output characteristics of sensing unit 2 is shown in Fig. 4a (ii). The voltage output of sensing unit 2 varies with a period of 90°, with 90° being the most sensitive direction. The impact of touch direction on the output characteristics of sensing unit 3 is shown in Fig. 4a (iii). As the touch direction increases from 0° to 360°, the voltage output of sensing unit 3 also varies with a period of 90°. The impact of touch direction on the output characteristics of sensing unit 4 is shown in Fig. 4a (iv). The voltage output of sensing unit 4 varies with a period of 90°, with 270° being the most sensitive direction compared to other sensing units. In order to avoid the phenomenon of different overall output levels of each sensing unit caused by human manufacturing errors and to more intuitively express the sensitivity of each sensing unit to the directional load, the maximum output voltage of each sensing unit is taken as its respective basic voltage V_{maxi}, and the voltage response caused by the directional load is normalized:

$$\Delta V_i = \frac{V_i}{V_{maxi}} \tag{13}$$

Where the ΔV_i represents the normalized characteristic value of the output voltage of the sensing unit i ($i = 1,2,3,4$). V_i represents the output voltage of sensing unit i caused by the current directional load. V_{maxi} represents the maximum voltage output of sensing unit i.

The response law of LTWS to the touch direction after normalization is shown in Fig. 4b. It can be clearly seen that LTWS has a high perception sensitivity to loads in different directions. Combined with the

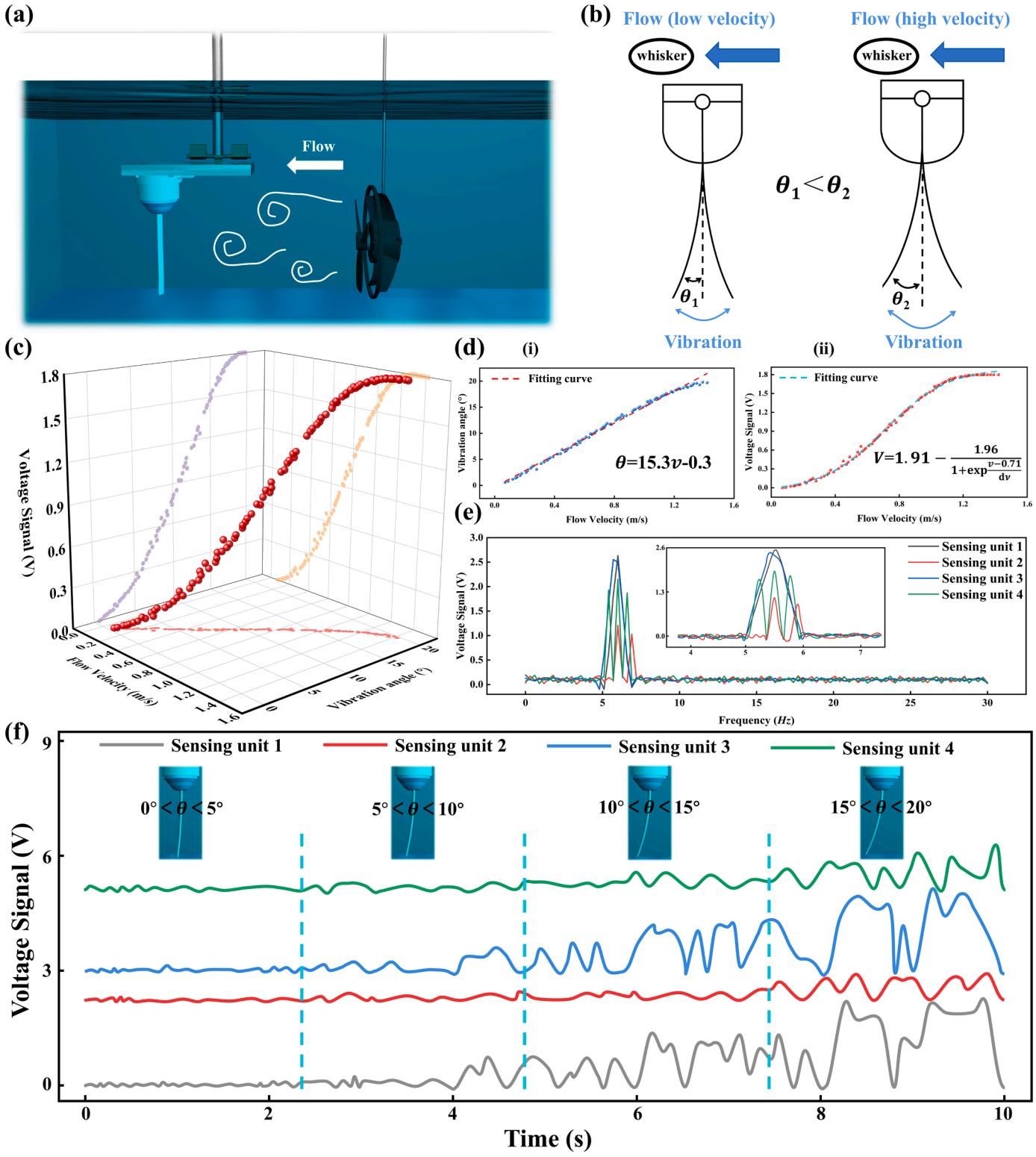

Fig. 5. Application of LTWS in flow velocity measurement. (a) Underwater speed measurement test bench of LTWS. (b) Schematic diagram of the effect of different flow velocity on the vibration amplitude of LTWS tentacles. (c) Three-dimensional scatter plot of the relationship between flow velocity, vibration angles and output voltage. (d) Fitting curve diagram of the relationship between flow velocity, vibration amplitude and output voltage. (e) The position diagram of the main vibration peak of each sensor unit in the spectrum analysis. (f) Signal output at different vibration angles caused by different flow velocity of LTWS.

voltage signal peak appearing on the rising edge or falling edge, the voltage response law after normalization can effectively distinguish the touch direction. The same change trend of the four sensing units fully verifies that the tentacle of LTWS have fully achieved elastic balance. At the same time, the overall structure of LTWS has high mechanical flexibility and stability. Therefore, the LTWS production process proposed in this paper has high feasibility and has the potential to be further applied in automated equipment, laying a good theoretical foundation for further realizing tactile perception.

To further verify the applicability and feasibility of the LTWS designed in this study, a program was developed using the Arduino development board to control the switch state of an LED light based on the LTWS output voltage (details are provided in Supplementary Material S2). By transmitting the voltage analog signal of the LTWS sensing unit to the Arduino development board, a demonstration experiment of LTWS real-time control of lighting up LED lights in different directions was realized. By writing a program to the Arduino development board, the voltage signals of the four sensing units of the LTWS can be collected in real time and the voltage values of the four channels can be transmitted to the computer interface for display. At the same time, the LTWS sensing unit can control the state of the LED light through voltage after setting the threshold voltage. The equivalent circuit diagram of this experiment is shown in Fig. 4c. The experimental bench required for the experiment is shown in Fig. 4d, which mainly includes LTWS, breadboard, Arduino development board, LED lights (four green, four blue), and a computer for writing code (not shown).

Fig. 4e (i) shows a real-time control demonstration using LTWS sensing unit 1 as an example. Initially, the whiskers of the LTWS are gently touched along the 0° direction, causing sensing unit 1 to generate a voltage response with a peak voltage that exceeds the 1 V threshold (threshold 1) but remains below the 1.5 V threshold (threshold 2), at this point, only one LED light is illuminated. Subsequently, as the touch offset amplitude of the whiskers is gradually increased, sensing unit 1 generates a voltage response exceeding 1.5 V. With the voltage surpassing threshold 2, both LED lights are illuminated. After this experiment, the LTWS tentacle were tested one by one along the directions of 90°, 180°, and 270°, and the results are shown in Fig. 4e (ii) - Fig. 4e (iv). It is evident that when the voltage value lies between threshold 1 and threshold 2, only one LED light is illuminated. However, when the voltage exceeds threshold 2, both LED lights are illuminated. The experiment can verify the LTWS's sensitive perception of different touch directions and touch offset amplitudes, as well as its potential in practical applications.

3.2. Application of LTWS in flow velocity measurement

In an underwater environment, LTWS can also sense the flow rate of the surrounding water based on the swing amplitude of its tentacle. To emulate operational conditions of an underwater robot carrying the LTWS, the sensor was mounted on a towed platform and the fore-mounted propeller speed was varied to generate different flow rates; the experimental bench is shown in Fig. 5a. It was observed that, at low flow velocity, impact-induced whisker deflections were minimal, whereas the vibration angle θ increased progressively with rising velocity, as shown in Fig. 5b. This phenomenon establishes a direct correlation between flow velocity and whisker vibration angle, enabling flow sensing via vibration amplitude. A series of experiments was conducted to quantify the relationship among flow velocity, whisker vibration angle, and output voltage. By adjusting flow speed and recording the corresponding θ and voltage outputs, a mathematical model for accurate velocity estimation was derived. As depicted in Fig. 5c, When the water flow velocity gradually increases from 0.2 m/s to 1.6 m/s, the vibration angle θ of the tentacle shows an obvious increasing trend, from the initial 0° to 20°. Meanwhile, the output voltage of LTWS also rises rapidly from 0.05 V to 1.80 V, and shows slight fluctuations in the high flow rate range. However, at higher flow velocities, the rate of increase for both parameters diminishes, and the curve tends to stabilize, deviating from the previously observed linear growth. This phenomenon is mainly attributed to three factors: nonlinear hydrodynamic effects, mechanical structure saturation, and liquid metal contact area saturation. Specifically, flow-induced turbulence and boundary layer separation reduce the effective hydrodynamic force acting on the whisker. Meanwhile, the carbon fiber whisker approaches its maximum elastic bending limit, constraining further deflection. Finally, the contact area between the liquid metal and silicone layers reaches saturation, limiting additional charge transfer and voltage output.

To further quantify the relationships among the three parameters, separate fits of flow velocity versus vibration angle and flow velocity versus output voltage were performed, the results of which are shown in Fig. 5d. By performing a linear fit on the θ–ν relationship, the following equation is obtained:

$$\theta = 15.3\nu - 0.3 \quad , \quad R^2 = 0.98175 \tag{14}$$

And the V–ν relationship was accurately described by a logistic model:

$$V = 1.91 - \frac{1.96}{1 + \exp^{\frac{\nu - 0.71}{d\nu}}} \quad , \quad R^2 = 0.97268 \tag{15}$$

Thereby providing explicit analytical expressions.

In addition, as shown in Fig. 5e, each sensing unit maintains a main vibration peak of about 5.5 *Hz* in the spectrum analysis, which not only shows the flow-induced vibration frequency of the fluid-tentacle coupling system, but also verifies the multi-channel and high-consistency design of LTWS, which is helpful to achieve high-precision underwater flow velocity perception and analysis. In order to verify the adaptability of LTWS in different flow velocity environments, the flow velocity was gradually increased from 0 m/s to 1.6 m/s according to the experimental results, and the time domain output voltage of the four sensing units was recorded synchronously, and the results are shown in Fig. 5f. When the flow velocity is 0–0.4 m/s, the tentacles only produce a slight swing of no more than 5°, and the corresponding voltage output is extremely low, as the flow velocity increases, the tentacle vibration angle and the output voltage of the four sensing units show an increasing trend, and the measured data in each angle range are highly consistent with the mathematical model obtained by the previous fitting. Due to the limitations of the LTWS manufacturing process and the rotation speed of the front propeller, the maximum vibration angle that can be measured in the current experiment is only 20°, with the subsequent optimization of materials and equipment, this range is expected to be further expanded. In summary, the existing data fully demonstrates the excellent consistency and synchronization between the system's multiple channels, and also clearly shows that LTWS can stably and accurately adapt to a variety of flow rate environments.

3.3. Simulate the motion perception experiment of AUV equipped with LTWS

To verify that the LTWS enables underwater tactile perception and can assist underwater robots in exploration and obstacle avoidance, the LTWS is mounted on an underwater towing system to simulate the scenario of an underwater robot equipped with the LTWS working underwater. The dual-axis towing system of the underwater robot is utilized to control the LTWS, allowing it to actively make contact with obstacles, thereby validating the underwater tactile perception capabilities of the LTWS.

The LTWS underwater experimental platform is shown in Fig. 6a, which mainly includes a large indoor pool (5 m×3 m×2 m), a towing system, three underwater obstacles, a signal acquisition box, a signal acquisition terminal, a towing system control terminal, etc. The complete experimental process is that the experimenter controls the LTWS carried by the towing platform through the underwater robot dual-axis

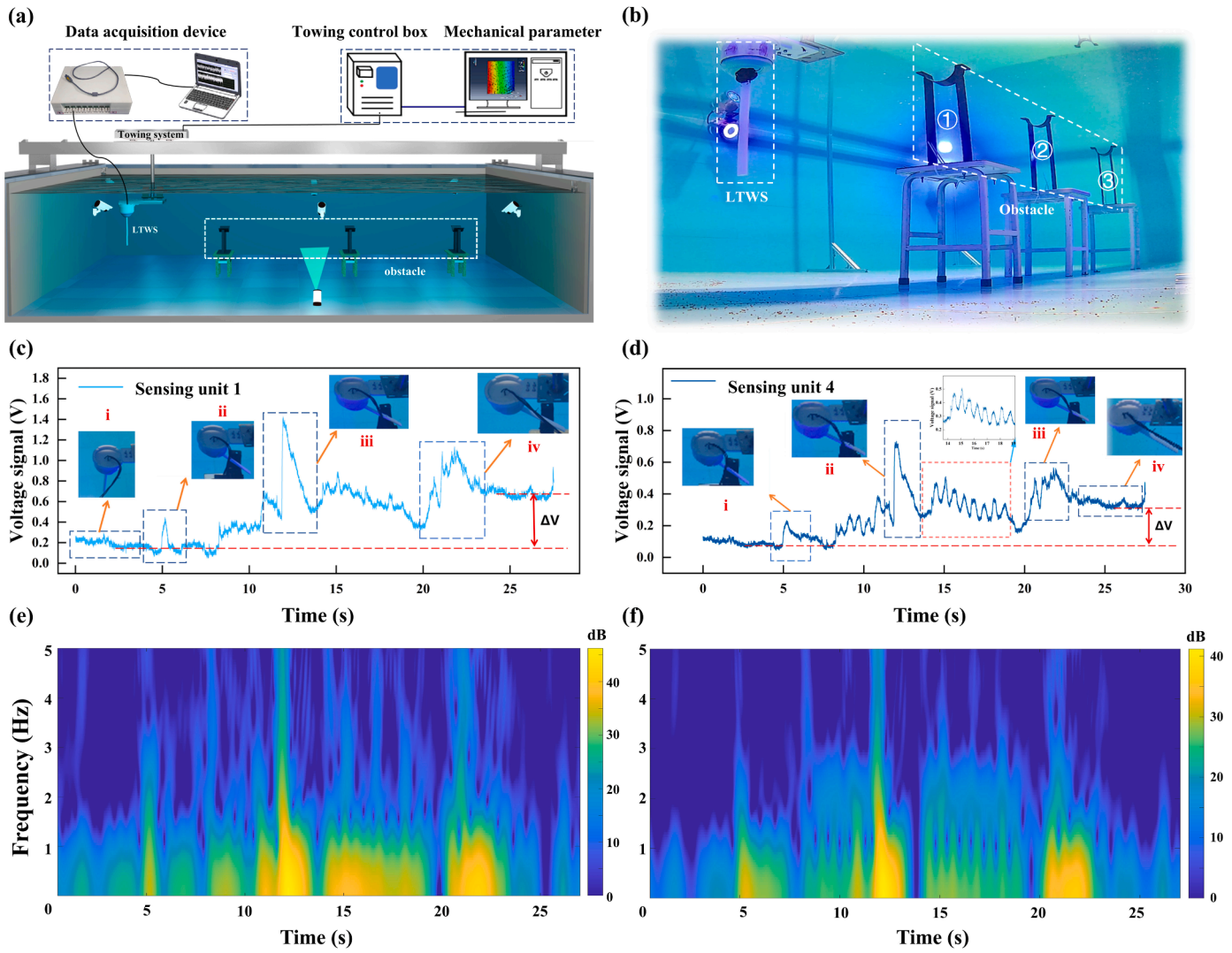

Fig. 6. Underwater sensing verification experiment of LTWS. (a) Underwater test bench of LTWS. (b) Real shot of LTWS underwater tactile perception test platform (underwater perspective). (c) Voltage signal response of LTWS sensing unit 1 in underwater tactile test. (d) Voltage signal response of LTWS sensing unit 4 in underwater tactile test. (e) Time-frequency signal energy diagram of LTWS sensing unit 1 in underwater tactile test. (f) Time-frequency signal energy diagram of LTWS sensing unit 4 in underwater tactile test.

towing system, and actively collides with the three obstacles placed in the path in turn at the pre-set travel speed and path. After the LTWS touches the obstacle, the sensing unit generates a voltage signal. Further, the signal transmission wire of the sensing unit is connected to the signal acquisition box, which reads the voltage signal and transmits it to the signal acquisition terminal in real time. During the experiment, the status of the LTWS underwater tactile perception test platform can also be observed in real time through the underwater camera placed at the bottom of the pool. Fig. 6b shows the test platform captured by the underwater camera, where the LTWS and the three underwater obstacles can be clearly seen. Since the deflection direction of the whiskers in the underwater tactile test of LTWS is 0°, which is the most sensitive load direction of sensing unit 1, sensing unit 1 is taken as an example to analyze the voltage signal generated during the underwater tactile test of LTWS. As shown in Fig. 6c, the voltage signal corresponding to serial number i is the starting stage. Since the movement amplitude of the whiskers is small when they do not touch the obstacle, the overall signal of sensing unit 1 is relatively stable in the starting stage; the voltage signal corresponding to serial number ii is the voltage signal generated by the whiskers colliding with the first obstacle, and obvious peaks can be observed; after the first collision, LTWS continues to move forward steadily, corresponding to the stable voltage signal before serial number iii, and then LTWS collides with the second obstacle, and the peak corresponding to serial number iii appears; the peak of LTWS whiskers colliding with the third obstacle is shown in serial number iv. It can be seen that LTWS has a sensitive perception of the collision with obstacles. Each collision with an obstacle will produce peaks as shown in serial numbers ii, iii, and iv, reflecting the external load stimulus in the electrical signal output. Therefore, in practical applications, we can determine whether the LTWS has collided based on the peak of the voltage signal, thereby enabling the underwater robot to acquire the ability to avoid underwater collisions.

To further verify the accuracy of the experimental results, an additional set of control experiments was conducted. Since sensing units 1 and 4 are on opposite sides, we took sensing unit 4 as the research object and carried out control experiments. The experimental results are shown in Fig. 6d, and its trend is exactly the same as that of sensing unit 1. Additionally, it is observed that after the three collision processes are completed, the final potential of sensing units 1 and 4 is higher than their initial potential, with a potential difference of ΔV between the two. This increase is due to the fact that the LTWS tentacle deflect to a certain angle toward 0° in the final stage and do not return to the center. This can be clearly demonstrated in the supplementary material S9. Fig. 6e and Fig. 6f show the frequency *STFT* analysis of the output voltage

signals from sensing unit 1 and sensing unit 4 respectively, during the underwater tactile experimental operation. The colors in the figure represent different signal strengths, and the signal strength gradually increases from blue to yellow. The signal strength unit is dB. As shown in these two figures, the distribution pattern of the strong signal aligns with the time-domain voltage waveform shown above. Notably, when the time-domain voltage exhibits a pronounced peak, the spectral energy at the corresponding moment in the time-frequency diagram concurrently increases, indicating a high degree of coupling between the output voltage amplitude and the mechanical vibration energy in the primary vibration mode. Furthermore, the primary spectral peaks from the two distinct channels are simultaneously activated at the same time point and frequency, demonstrating the synchronous response and consistency among multiple channels within the LTWS system. In addition, the voltage difference ΔV observed before and after the collision experiments is not caused by the collisions but rather by the residual static deflection of the whisker. Therefore, it cannot be clearly reflected in the time–frequency analysis as a collision-related energy enhancement. In summary, LTWS showed good obstacle collision detection ability in the underwater tactile test, and can obtain information through the touch of the tentacle with obstacles underwater, which verifies that LTWS has good underwater tactile perception ability.

4. Conclusions

Drawing inspiration from the structure of sea otter whisker follicles, this paper presents liquid metal, known for its high conductivity, fluidity, and electrode self-repairing properties, as both the triboelectric and electrode layers in a triboelectric nanogenerator-based self-powered sensing technology. An innovative bionic tentacle-type liquid metal-based triboelectric whisker sensor LTWS is proposed. Following comprehensive experimental validation and data analysis, the sensor can achieve high sensitivity perception of tactile information, with a measured sensitivity of 7.9 mV/mm in static offset deflection experiments. Meanwhile, the actual application scenario of underwater robots equipped with LTWS is simulated to verify the underwater tactile perception ability of LTWS, with the sensor reliably detecting underwater collisions and distinguishing three distinct events through characteristic voltage peaks in the time domain and corresponding energy enhancements in the time–frequency domain.

The main research work of this paper is summarized and concluded as follows: (1) Under identical load conditions, the liquid metal–hydrogel electrode exhibits a 33.8 % increase in output signal and a 28.9 % improvement in response time compared to the conductive ink–FEP film electrode, demonstrating the superior performance of the liquid metal–hydrogel electrode. (2) Once the upper and lower electrodes of the contact-separation triboelectric nanogenerator are fabricated, the induced potential difference V and charge transfer Q are directly correlated with the distance between the triboelectric layers. (3) The data from the underwater flow velocity measurement experiments reveal a clear mathematical relationship among flow velocity, tentacle vibration angle, and output voltage, expressed in the range of 0.2–1.6 m/s, with sensing units oriented perpendicular to the flow producing larger and more dynamic output signals compared to those aligned with the flow. This relationship allows for the derivation of any one of these parameters given the other two. (4) The data from the lighting experiment and underwater simulation experiment demonstrate the LTWS's sensitive perception of different touch directions and touch offset amplitudes, with the four sensing units arranged at 0°, 90°, 180°, and 270° clearly distinguishing directional inputs. This indicates that the LTWS can effectively enrich the perception dimension of AUVs. Overall, the LTWS can convert the difficult-to-measure mechanical motion of carbon fiber tentacle into quantifiable electrical signals. In marine environments with low visibility and high self-noise, it can supplement underwater optical and sonar detection systems, thereby enhancing the environmental perception capabilities of underwater robots. This allows these robots to acquire multimodal oceanic information, enriching their perception dimension.

CRediT authorship contribution statement

Yuanzheng Li: Writing – original draft, Visualization, Software, Methodology, Formal analysis, Data curation, Conceptualization. **Liguo Song:** Writing – review & editing, Visualization, Methodology, Funding acquisition, Formal analysis. **XU MINYI:** Writing – review & editing, Visualization, Methodology, Funding acquisition, Formal analysis, Conceptualization. **Xirui Dai:** Writing – review & editing, Formal analysis, Data curation, Conceptualization. **Jianhua Liu:** Writing – review & editing, Formal analysis, Data curation, Conceptualization. **Hao Jin:** Software, Methodology, Funding acquisition. **Weichao He:** Software, Methodology, Funding acquisition. **Peng Xu:** Writing – review & editing, Visualization, Methodology, Funding acquisition, Formal analysis. **Kecheng Zhang:** Methodology, Investigation. **Zinan Guo:** Methodology, Investigation. **Tianrun Wang:** Methodology, Investigation. **Xinyue Zhou:** Methodology, Investigation.

Declaration of Competing Interest

All the contributing authors report no conflict of interests in this work.

Acknowledgements

Yuanzheng Li, Jianhua Liu, and Xirui Dai contributed equally to this work. This work was supported in part by the National Natural Science Foundation of China [52371345, 52401399, 52071046]; the Xingliao Talent Plan Young Talent Project of Liaoning Province [XLYC2203175]; Scientific Research Innovation Capability Support Project for Young Faculty [ZYGXQNJSKYCXNLZCXM-O1P], and the Postdoctoral Fellowship Program of China Postdoctoral Science Foundation [GZC20230062].

Appendix A. Supporting information

Supplementary data associated with this article can be found in the online version at doi:10.1016/j.sna.2025.116917.

Data availability

Data will be made available on request.

References

[1] C. Cheng, C. Wang, L. Gao, F. Zhang, OCEANS 2018 MTS/IEEE Charleston, IEEE, 2018, pp. 1–4.
[2] K. Kebkal, A. Kebkal, E. Glushko, V. Kebkal, L. Sebastião, A. Pascoal, J. Ribeiro, H. Silva, M. Ribeiro, G. Indiveri, Gyroscopy Navig. 10 (2019) 313–321.
[3] N. Tsiogkas, G. Frost, N. Monni, D. Lane, Facilitating multi-AUV collaboration for marine archaeology. OCEANS 2015-Genova, IEEE, 2015, pp. 1–4.
[4] Y. Zhang, W. Ge, Auv path planning and image recognition based on convolutional neural network, in: 3rd International Conference on Big Data, Artificial Intelligence and Internet of Things Engineering (ICBAIE), 2022, IEEE, 2022, pp. 605–608.
[5] M.V. Jakuba, O. Pizarro, S.B. Williams, High resolution, consistent navigation and 3D optical reconstructions from AUVs using magnetic compasses and pressure-based depth sensors. OCEANS'10 IEEE SYDNEY, IEEE, 2010, pp. 1–9.
[6] T. Kasaya, Y. Nogi, K. Kitada, Explor. Geophys. 54 (2) (2023) 205–216.
[7] C. Kunz, H. Singh, Stereo self-calibration for seafloor mapping using AUVs. IEEE/OES Autonomous Underwater Vehicles, IEEE: 2010, 2010, pp. 1–7.
[8] Y. Li, B. Liu, P. Xu, J. Liu, X. Dai, A. Yu, T. Wang, L. Guo, T. Guan, L. Song, Nano Res. 17 (11) (2024) 10008–10016.
[9] Y. Nan, F. Long, F. Yun, S. Yao, L. Wang, C. Li, P. Wang, M. Liu, Z. Li, J. Mar. Sci. Eng. 10 (6) (2022) 715.
[10] Liu, B.; Dong, B.; Jin, H.; Zhu, P.; Mu, Z.; Li, Y.; Liu, J.; Meng, Z.; Zhou, X.; Xu, P., Advanced Materials Technologies, 2401053.
[11] Q. Qiao, X. Kong, S. Wu, G. Liu, G. Zhang, H. Yang, W. Zhang, Y. Yang, L. Jia, C. He, Remote Sens. 15 (11) (2023) 2949.
[12] P. Xu, J. Liu, B. Liu, Y. Li, H. Jin, Z. Mu, T. Guan, G. Xie, H. Wang, M. Xu, Nano Energy 129 (2024) 110011.

[13] J. He, J. Wen, S. Xiao, J. Yang, IEEE/CAA J. Autom. Sin. 10 (3) (2023) 828–830.
[14] Y. Tipsuwan, P. Hoonsuwan, Design and implementation of an AUV for petroleum pipeline inspection. 7th International Conference on Information Technology and Electrical Engineering (ICITEE), IEEE: 2015, 2015, pp. 382–387.
[15] H. Zhang, S. Zhang, Y. Wang, Y. Liu, Y. Yang, T. Zhou, H. Bian, Appl. Ocean Res. 107 (2021) 102321.
[16] Y. Li, T. Wang, T. Guan, P. Xu, H. Wang, M. Xu (in Chinese), J. Underw. Unmanned Syst. 32 (2024) 1–8.
[17] D.Q. Huy, N. Sadjoli, A.B. Azam, B. Elhadidi, Y. Cai, G. Seet, Ocean Eng. 267 (2023) 113202.
[18] S.M. Zadeh, D.M. Powers, K. Sammut, Robot. Auton. Syst. 87 (2017) 81–103.
[19] M. Doron, M. Babin, A. Mangin, O. Hembise, J. Geophys. Res. Oceans 112 (C6) (2007).
[20] G.M. Wenz, J. Acoust. Soc. Am. 51 (3B) (1972) 1010–1024.
[21] P.C. Chu, C. Fan, J. Appl. Remote Sens. 13 (4) (2019), 047502-047502.
[22] J.S. Jaffe, K.D. Moore, J. McLean, M.P. Strand, Oceanography 14 (3) (2001) 66–76.
[23] S. Wang, W. Wu, X. Wang, Y. Han, Y. Ma, Underwater optical image object detection based on YOLOv7 algorithm. OCEANS 2023-Limerick, IEEE, 2023, pp. 1–5.
[24] Q. Chen, A. Mathai, X. Xu, X. Wang, A study into the effects of factors influencing an underwater, single-pixel imaging system's performance, Photonics MDPI (2019) 123.
[25] B. Cochenour, L. Mullen, A. Laux, Spatial and temporal dispersion in high bandwidth underwater laser communication links. MILCOM 2008-2008 IEEE Military Communications Conference, IEEE, 2008, pp. 1–7.
[26] X. Wang, Q. Li, J. Yin, X. Han, W. Hao, Remote Sens. 11 (4) (2019) 396.
[27] T. Zhou, J. Si, L. Wang, C. Xu, X. Yu, IEEE Trans. Geosci. Remote Sens. 60 (2022) 1–12.
[28] J.A. Catipovic, IEEE J. Ocean. Eng. 15 (3) (1990) 205–216.
[29] K. Tu, T.M. Duman, M. Stojanovic, J.G. Proakis, IEEE J. Ocean. Eng. 38 (2) (2012) 333–346.
[30] G.B. Bauer, R.L. Reep, C.D. Marshall, Int. J. Comp. Psychol. 31 (2018).
[31] P. Godfrey-Smith, Other minds: The octopus, the sea, and the deep origins of consciousness, Farrar, Straus and Giroux, 2016.
[32] S.M. Strobel, J.M. Sills, M.T. Tinker, C.J. Reichmuth, J. Exp. Biol. 221 (18) (2018) jeb181347.
[33] P. Xu, J. Liu, X. Liu, X. Wang, J. Zheng, S. Wang, T. Chen, H. Wang, C. Wang, X. Fu, npj Flex. Electron. 6 (1) (2022) 25.
[34] J. Liu, P. Xu, B. Liu, Z. Xi, Y. Li, L. Guo, T. Guan, P. Zhu, Z. Meng, S. Wang, Small 20 (19) (2024) 2308491.
[35] Z.L. Wang, Faraday Discuss. 176 (2014) 447–458.
[36] G. Zhu, B. Peng, J. Chen, Q. Jing, Z.L. Wang, Nano Energy 14 (2015) 126–138.
[37] Z. Gao, S. Wu, Y. Wei, M. Ibrahim, H.N. Abdelhamid, G. Jiang, J. Cao, X. Sun, Z. Wen, Holistic and localized preparation methods for triboelectric sensors: principles, applications and perspectives, Int. J. Extrem. Manuf. 6 (5) (2024) 052002.
[38] J. Yi, S. Liu, Z. Gao, S. Wu, H. Ji, J. Hou, G. Jiang, X. Sun, Z. Wen, A battery-free wireless sensor for encrypted signal transmission via Maxwell's displacement current, Microsyst. Nanoeng. 11 (1) (2025) 130.
[39] Daeneke, T.; Khoshmanesh, K.; Mahmood, N.; De Castro, I.A.; Esrafilzadeh, D.; Barrow, S.J.; Dickey, M.D.; Kalantar-Zadeh, K., Chemical Society Reviews 2018, 47 (11), 4073-4111.
[40] M. g Kim, H. Alrowais, S. Pavlidis, O. Brand, Adv. Funct. Mater. 27 (3) (2017) 1604466.
[41] J.-Y. Gao, S. Chen, T.-Y. Liu, J. Ye, J. Liu, Mater. Today 49 (2021) 201–230.
[42] S. Wang, P. Xu, X. Wang, J. Zheng, X. Liu, J. Liu, T. Chen, H. Wang, G. Xie, J. Tao, Nano Energy 97 (2022) 107210.

Yuanzheng Li is pursuing the Ph.D. degree in Dalian Maritime University, China. His current research interests are the Underwater tactile sensor based on triboelectric nanogenerator.

Jianhua Liu is currently pursuing his Ph.D. degree in Dalian Maritime University, China. His current research interests include underwater biomimetic sensor design, self-powered system and control, and triboelectric nanogenerator.

Xirui Dai is a junior student from the College of Marine Engineering at Dalian Maritime University. She has obtained the qualification for postgraduate recommendation.

Peng Xu received his Ph.D. degree from Dalian Maritime University, China. He is currently a post-doctoral fellow in the in dynamics and control with the College of Engineering, Peking University. His current research interests include self-powered sensing system and control, bio-inspired design and control for marine and underwater robots and triboelectric nanogenerators.

Liguo Song received the Ph.D. degree from Dalian Maritime University, Dalian, China, in 2020. Now, he is a Professor at the Marine Engineering College, Dalian Maritime University. He currently holds a certificate for the chief engineer of vessels of 3000 kW and above in unrestricted areas. His current research is mainly focused on the areas of marine pollution control, triboelectric nanogenerators and its practical applications in smart ship and ocean.

Minyi Xu received his Ph.D. degree from Peking University in 2012. During 2016–2017, he joined Professor Zhong Lin Wang' group at Georgia Institute of Technology. Now he is a Professor in the Marine Engineering College, Dalian Maritime University. His current research is mainly focused on the areas of blue energy, self-powered systems, triboelectric nanogenerators and its practical applications in smart ship and ocean.